

## 2D electron density profile evolution during detachment in Super-X divertor L-mode discharges on MAST-U

N. Lonigro<sup>1,2</sup>, R. S. Doyle<sup>2,3</sup>, K. Verhaegh<sup>2</sup>, B. Lipschultz<sup>1</sup>, D. Moulton<sup>2</sup>, P. Ryan<sup>2</sup>, J. S. Allcock<sup>2</sup>, C. Bowman<sup>2</sup>, J. Harrison<sup>2</sup>, S. Silburn<sup>2</sup>, C. Theiler<sup>4</sup>, T.A. Wijkamp<sup>5</sup>, the WPTE Team and MAST-U Team

<sup>1</sup>York Plasma Institute, University of York, United Kingdom

<sup>2</sup>UKAEA, Culham Science Centre, United Kingdom

<sup>3</sup>NCPST, Dublin City University, Ireland

<sup>4</sup>Ecole Polytechnique Federale de Lausanne (EPFL), Swiss Plasma Center (SPC), Switzerland

<sup>5</sup>DIFFER, Eindhoven, Netherlands

E-mail: nicola.lonigro@ukaea.uk

*Keywords:* CIS, Coherence Imaging, Stark broadening, MAST Upgrade, Super-X divertor

**Abstract.** 2D electron density profiles obtained from coherence imaging spectroscopy in different MAST-U divertor conditions are compared. The data includes variations of strike point position, core electron density, and heating power. The improved performance of the long-legged divertors results in a lower electron density and particle flux at the target compared to configurations with smaller strike point major radius, while also being characterized by lower temperatures and deeper detachment. Comparisons against SOLPS simulations generally show good agreement in profile shape along and across the separatrix. The peaking of the electron density downstream of the detachment front is associated with significant neutral drag acting on the plasma flow.

### 1 Introduction

Future tokamak fusion reactors are designed to generate a large amount of power. If unmitigated, a significant fraction of this power would be concentrated in a thin toroidal ring when reaching the walls of the device, with expected widths on the order of several millimeters [1], and the associated heat fluxes on the divertor targets would surpass material limits. Thus, reactors will need to operate in detached divertor conditions to ensure enough volumetric particle, power and momentum losses occur to reduce the heat flux on the target. Understanding detachment, and being able to correctly model it, is then imperative to correctly extrapolate the behaviours of current experiments to future reactors.

Alternative divertor configurations are being studied to improve access to detachment and maintain good core performance in a detached divertor state. Some examples include the X divertor[2], the Snowflake divertor[3], the Super-X divertor[4] and the X-point target divertor[5]. Devices with flexible divertors, such as TCV[6][7] and MAST-U [8],[9][10], are particularly useful in comparing many different divertor configurations in similar core plasma conditions. The MAST-U Super-X divertor combines the advantages of large total flux expansion with a long scrape-off layer path through the strongly baffled divertor chamber, increasing dissipative plasma-neutral interactions. It has shown a strong improvement in exhaust performance when compared to more conventional divertors[11], in accordance with modelling[12]. Experiments on the Super-X divertor

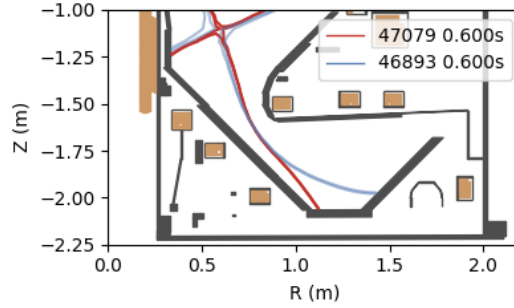


Figure 1: Range of divertor configurations scanned in this work. Taken from EFIT magnetic reconstructions at  $t = 0.6$  s of the core density ramps in elongated divertor #47079 and Super-X divertor #46893.

on TCV have shown no significant improvements in a non-baffled configuration [13] and only modest improvements in a baffled configuration when compared to simple analytical scaling [14]. The effect of strong plasma flows on the benefits of flux expansion and the related momentum losses has been proposed as a partial explanation for part of this discrepancy [15].

Previous work on the MAST-U Super-X divertor has focused on the increased access to detachment, the stability of the detachment front and the particle balance [10] as well as the increase in molecular rotational temperature during detachment [16]. In this work, the 2D electron density profiles obtained with the new multi-delay coherence imaging diagnostic [17] are studied in a variety of experimental conditions and compared against models to determine the influence of plasma shaping on the divertor electron density behaviour and its evolution in deeply detached conditions in a strongly baffled divertor. The diagnostic uses interferometric imaging techniques to obtain Stark broadening information of the deuterium (D) gamma spectral line, which is directly related to the electron density. This information is then used to infer 2D poloidal profiles under the assumption of toroidal symmetry, enabling detailed studies on the electron density profile evolution both along the separatrix and across the fieldlines. Details on inference the technique, validation on synthetic data and comparison against other diagnostics have been previously reported [18]. In section 2, an overview of the MAST-U device is given and the divertor configurations of interest for this paper are shown. In section 3 the 2D profile measurements are shown in a variety of L mode conditions. These include a sweep of the strike point position, core density ramps, and discharges with different input powers. These measurements are discussed and compared to models in section 4.

## 2 MAST-U Discharges overview

MAST-U is a medium sized spherical tokamak with major radius  $R = 0.9$  m and minor radius  $a = 0.6$  m. All the discharges in this work have a toroidal field on axis of 0.65 T and a plasma current of 750 kA. Fuelling is performed from the low field side to inhibit access to H mode. Working in L mode prevents ELMs, thus simplifying the study of the density profile evolution using the coherence imaging diagnostic, which in the 2nd MAST-U campaign operated with a framerate of 30 Hz. The divertor leg is scanned from the elongated divertor (ED) magnetic configuration to the Super-X (SXD) divertor configuration, both in a symmetric double-null configuration, as shown in figure 1. Some details on the divertor magnetic geometries are given in figure 2, where the connection

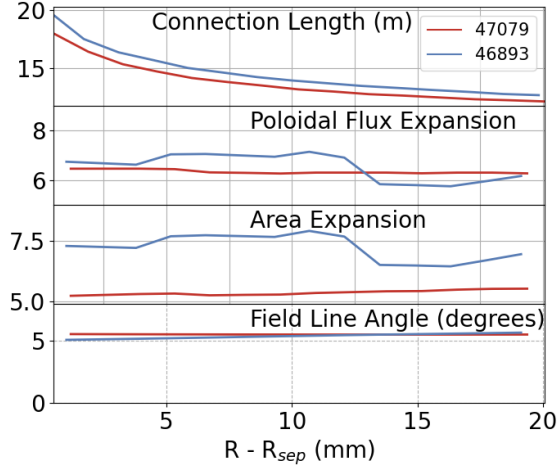


Figure 2: Divertor geometry parameters at the target in ED(#47079) and SXD(#46893).

length, poloidal flux expansion, cross-field area expansion (due to total flux expansion, compared to the midplane) and total field line angle at the target are compared. The SXD has a longer connection length, as well as a larger poloidal flux expansion and area expansion. The strike point field line angle with the target is comparable between the two geometries. Core density ramps have been performed in ED and SXD to study the evolution of the electron density profiles with increasing depths of detachment at the two extremes of the scanned target major radius range. An ohmic core density ramp in SXD is also analyzed to study more deeply detached conditions. The Elongated and Super-X divertor are never attached in the experimental range examined in this work. The minimum core density achievable in the core density ramps is set by the onset of MHD activity, which manifests itself in the divertor in the form of strike point splitting[19]. The discharges discussed in this work are

- #48140 Ohmic core density scan in Super-X divertor configuration
- #46893 Beam-heated core density scan in Super-X divertor configuration
- #47079 Beam-heated core density scan in Elongated divertor configuration
- #46895 Beam-heated strike point radius scan with constant upstream conditions

An overview of the core parameter evolution during these shots is shown in figure 3. The long-legged divertor shapes are established at 0.45 s, and the scanned range of the line-averaged core electron density is comparable in the different density ramps,  $2-4 \cdot 10^{19} m^{-3}$ . This corresponds to a range of [25 % , 50 %] in Greenwald density fraction. The core electron density is kept constant during the divertor leg scan, albeit the divertor pressure keeps increasing during the discharge. The NBI power is slightly higher in the SXD core density ramp, 1.7 MW, compared to the 1.5 MW in the ED core density ramp and the shape scan. The Ohmic discharge has no additional NBI power.

### 3 Electron density profiles measurements

MAST-U combines state of the art diagnostic techniques, such as multi-delay coherence imaging and multi-wavelength imaging, with a long divertor leg in a large and open divertor chamber. The

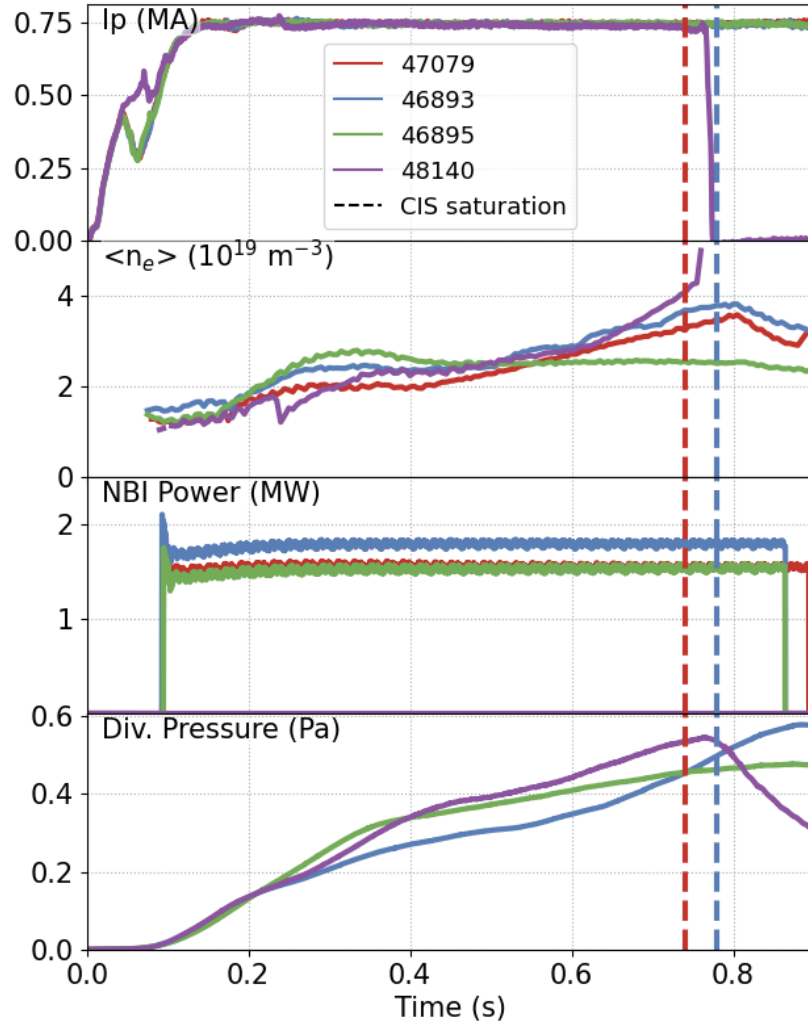


Figure 3: Overview of core parameters (Plasma current, line averaged density, injected NBI power) and divertor pressure in the discharges analyzed in this work. The vertical dashed lines show the time at which the CIS camera saturates in discharges #47079 and #46893. No divertor pressure measurements are available in #47079.

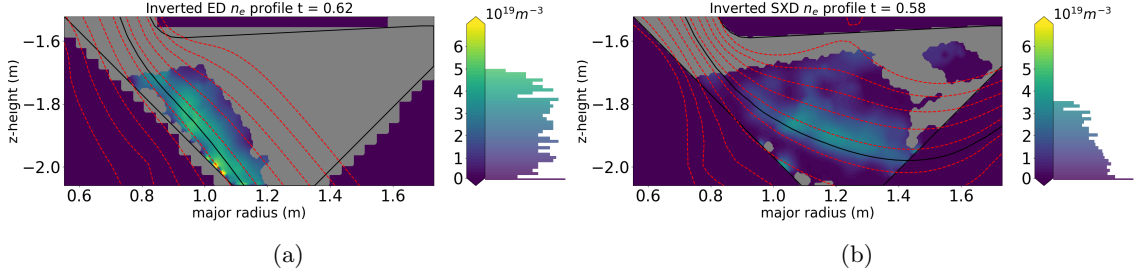


Figure 4: 2D electron density profile in (a) ED core density ramp #47079 and (b) SXD core density ramp #46893 at 40 % Greenwald fraction. The separatrix is shown in black. The masked off region has an emissivity  $\leq 10\%$  of its maximum.

long connection length and wide divertor chamber makes it easier to diagnose compared to more compact baffled designs, reducing requirements on spatial resolution and allowing detailed studies of the divertor behaviour along the separatrix. The electron density is one of the basic parameters describing the divertor state, with most of the processes driving detachment, power and momentum losses having electron density dependencies. This work will focus on characterizing the evolution of this fundamental parameter, before moving on to the evolution of derived quantities in future work. In particular, there is a focus on the behaviour of the electron density in detached conditions, which will be required for the safe operation of future devices.

### 3.1 Evolution during detachment

The behaviour of the density profiles with increased depth of detachment can be compared at the two extremes of the scanned divertor leg strike point range using core density ramps with fixed divertor shapes and similar core conditions. The SXD and ED divertor plasmas are already detached at the start of the discharge, but as the core density increases the divertor plasmas evolve as the electron temperature decreases further [11]. Towards the end of the discharge, as the plasma emission increases significantly due to the onset of electron-ion recombination emission, the CIS camera saturates. Thus, the density profiles could only be reconstructed for a part of the density scans, as shown in figure 3 with dashed vertical bars. A comparison of the 2D electron density profiles for the same core Greenwald fraction of 40% are shown in figure 4. The electron density is higher in the ED compared to the SXD and the spatial profile is mostly flat in both configurations.

The evolution of the density profiles during the density ramp along the separatrix determined by EFIT are shown in figure 5 for the two discharges, along with the position of the 50 % falling edge ("emission front") for the  $D_2$  Fulcher band emission along the separatrix, used as a proxy for the detachment front location [9][10]. The spatial profile along the separatrix is flat for most of the divertor chamber in both configurations, while significant density changes are observed close to the target. At the lowest core densities, the density profiles are non-monotonic, slightly decreasing between the detachment front and the target. As the core density increases, the spatial profile flattens and then starts peaking towards the target at even higher core densities. The density peak is not observed to detach from the target even in the most detached conditions accessed in this discharge. In figure 6, the evolution of the cross-field electron density profiles during the ED and SXD scans are shown in normalized  $\psi$  space at 3 cm from the target, to avoid possible inversion artifacts that can develop close to the target tiles [18]. As the core and target density increase,

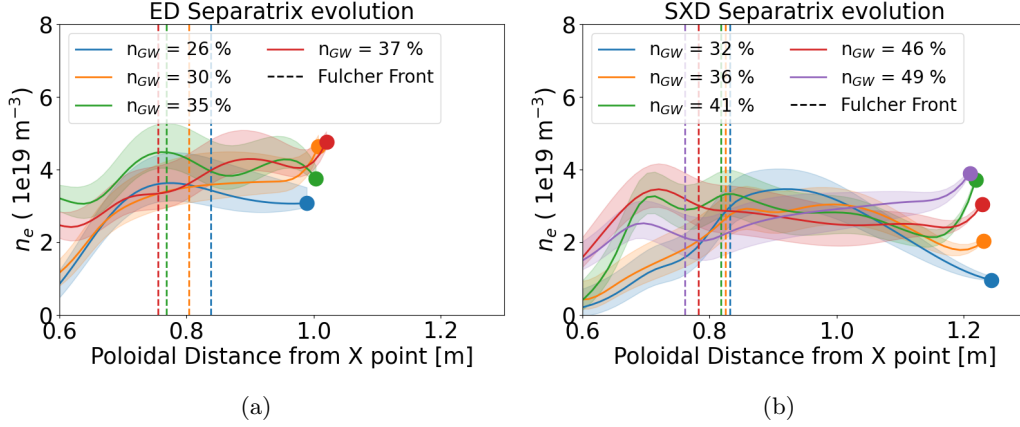


Figure 5: Separatrix evolution in (a) ED core density ramp #47079 and (b) SXD core density ramp #46893. The 50 % falling edge of the Fulcher emission along the separatrix is plotted as vertical lines.

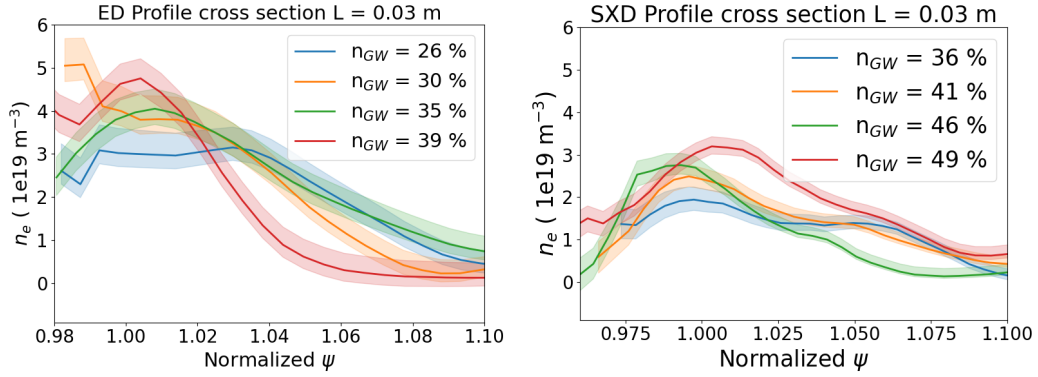


Figure 6: Separatrix cross-field electron density profiles (a) during the ED density scan and (b) SXD density scan at 3 cm from the target.

the spatial profile in the ED configuration becomes more peaked ( $\bar{\psi} \sim 1.01$ ). A high density is inferred in the private flux region, which is attributed to the proximity of the divertor leg to the neighbouring tile, but it is unclear if this is a real effect or an artifact of the inversion. In the SXD, the profile initially becomes more peaked, but then starts broadening again towards the end of the discharge, behaviour which could be preceding the detachment of the electron density front from the target.

A direct comparison between the two shapes can also be made. The density on the separatrix at 3cm from the target is taken as a proxy for the target density and it is plotted for both configurations as a function of upstream density in figure 7. The shaded area highlights the region as a function of Greenwald fraction for which overlapping density data is available. Both datasets are fit with a second-order polynomial. A comparison of the normalized cross-field profile in the ED and SXD configurations at the same upstream density (40 % Greenwald fraction) is also shown as a function of poloidal flux, normalizing the profiles by their values at the separatrix ( $\psi = 1$ ). The target density density is consistently higher in ED, with typical target densities two times as large as in

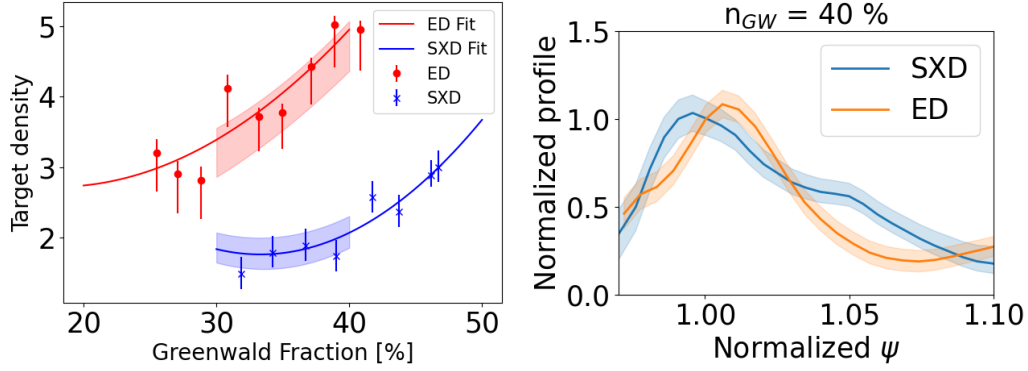


Figure 7: Evolution of separatrix electron density at 3cm of poloidal distance from the target in ED (#47079) and SXD (#46893) (b) in the SXD and ED at the same core density (35 % Greenwald fraction).

the SXD. This could be attributed to the previously reported particle sinks present in the additional divertor volume available in the SXD[20]. Both ED and SXD target densities increase by a factor  $\sim 50\%$  as the upstream density increases by  $\sim 50\%$  during the ramp. Regions further away from the target, in the middle of the divertor chamber, do not show a strong variation in density throughout the discharge. Comparing the cross-field profiles in the two configurations shows a broader electron density profile in the SXD for the same upstream density even when plotting the profiles against poloidal flux and thus accounting from the expected broadening in real space due to flux expansion. This is suggestive of additional cross-field transport in the SXD compared to the ED, attributed to the additional leg length.

### 3.2 Variation with strike point radius

In discharge #46895 the outer strike point radius is slowly swept from an Elongated to a Super-X configuration in L-mode to study the effect of changing magnetic geometry on the divertor behaviour for constant core parameters. The discharge has 1.5 MW of NBI power and a constant upstream density of  $\sim 30\%$  Greenwald fraction. The electron density profiles inferred by CIS as the leg moves from ED to SXD along the EFIT separatrix are shown in figure 8 as a function of distance from the X-point. The target position is shown as with a dot marker. The target electron density can be seen to decrease with increasing strike point radius, albeit it appears to start raising again in the latest stages of the discharge, which is possibly due to the continuously increasing divertor pressure. Similarly to the core density ramps, the divertor plasma is always detached in the scanned range. A non-monotonic electron density profile is inferred throughout the discharge, as observed in the initial stages of the core density ramps and in agreement with the low core density of this discharge. An interesting feature is that the density profiles appear to lay on top of each other when expressed in terms of distance from the X-point. This is in agreement with previous results showing that the Fulcher emission front (proxy for the  $\sim 5$  eV front position) remains in the same position when scanning the divertor leg[11], suggesting that (once it is off the target) the thermal front position is only a function of the magnetic geometry upstream of it, in agreement with simplified models [21][22]. The behaviour of the profiles inferred by CIS seems to suggest that something similar might apply for the electron density, likely due to similar particle losses (recombination) and source

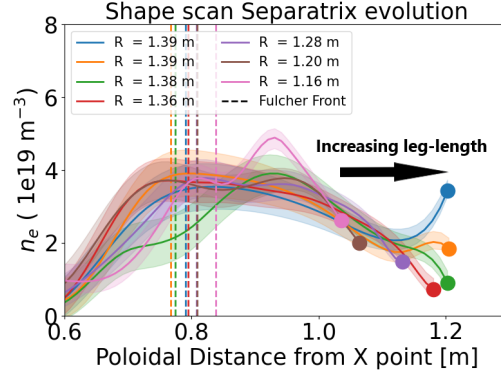


Figure 8: Separatrix density evolution in poloidal leg length scan #46895.

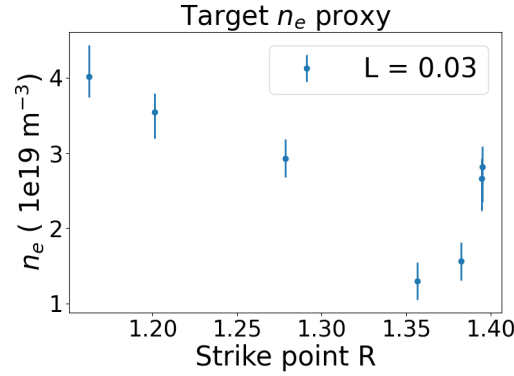


Figure 9: Target density in strike point scan #46895.

(ionization) terms as a function of distance from the X-point. In figure 9 the evolution of the separatrix density at 3 cm from the target is shown, here used as proxy for the target density. As the leg sweeps out, the electron density near the target decreases linearly with strike point major radius. The higher target density at a major radius of 1.4 m is associated with the separatrix crossing between two tiles, possibly due to an increase in the angle between the recycling neutrals and the separatrix leading to stronger plasma-neutral interactions.

### 3.3 Density front detachment in lower power conditions

The behaviour of the electron density profile under more deeply detached conditions can be studied by comparing the NBI heated core density ramp ( $P_{SOL} \sim 1.2$  MW) to an Ohmic density ramp ( $P_{SOL} \sim 0.5$  MW), where no additional external heating source is used during the discharge. The electron density profile along the separatrix during the Ohmic core density ramp #48140 is shown in figure 10. The first difference that can be noticed is the generally lower electron density, correlated to the lower power crossing the separatrix. The density profile is initially peaked at the target, as observed in the most detached stages of the NBI heated ramps. It then slightly increases before the density front detaches from the target and moves further upstream, leaving a region of low density behind ( $\leq 1 \cdot 10^{19} \text{ m}^{-3}$ ).



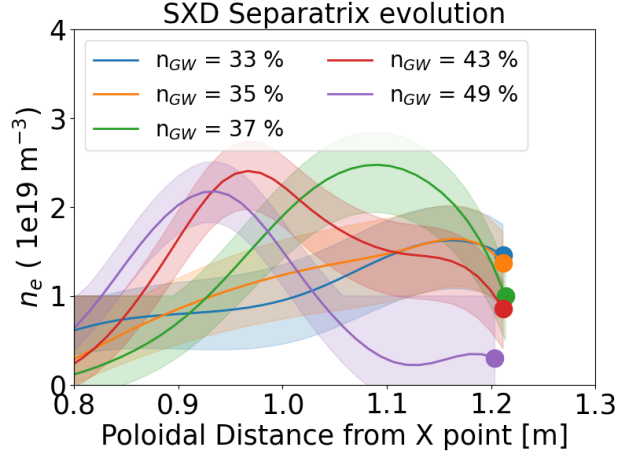


Figure 10: Separatrix density evolution during Ohmic core density ramp #48140.

## 4 Discussion

### 4.1 Density front detachment

The behavior of the electron density profiles can be compared to different markers of detachment to get a more complete picture of the divertor evolution. In the early stages of detachment the density profile is non-monotonic when expressed as a function of poloidal distance from the X-point. The maximum along the separatrix appears to be loosely correlated to the ionization front in the beam-heated discharges. This is similar to what was observed in predictive SOLPS-ITER simulations of the SXD divertor with ion-molecule collisions turned off [23], where the electron density profile peaks at the detachment front and then starts decreasing toward the target. As the divertor becomes more detached, the experimentally inferred density profiles flatten, becoming more peaked toward the target. This is more in agreement with the set of simulations that includes the ion-molecule collisions, which result in a flattening of the density profile near the ionization front and a build-up of density near the target.

This is reminiscent of behaviours observed in JET and TCV, where the density roll-over at the target is observed with a delay with respect to the ion flux rollover [24][25], suggesting that the peak in electron density profile should be downstream of the detachment front. A significant difference is that in JET the region of peak density along the profile moves from the target to the X point shortly after the detachment onset, resulting in a decreasing density from the X point to the target [24][26]. Instead, in MAST-U the density profile remains peaked at the target for most of the scanned range in upstream density and only detaches from the target in the most strongly detached conditions. An increased influence of ion-molecule collisions in later stages of the discharge could be expected by the constantly increasing neutral pressure in the divertor during the density ramp. In simulations, the density build-up is also associated with a drop in the plasma parallel velocity, which will be topic of future studies using coherence imaging flow measurements.

The detachment of the density front in Ohmic conditions can be compared to the four stages of detachment defined by Verhaegh et al. in similar Ohmic density ramps [10]. In particular, as shown in figure 11, the detachment of the density front ( $\sim 37\% n_{GW}$ ) precedes the detachment of the  $6 \rightarrow 2$  Balmer line emission front at  $\sim 43\% n_{GW}$  (as measured by the MWI diagnostic [27][19]),

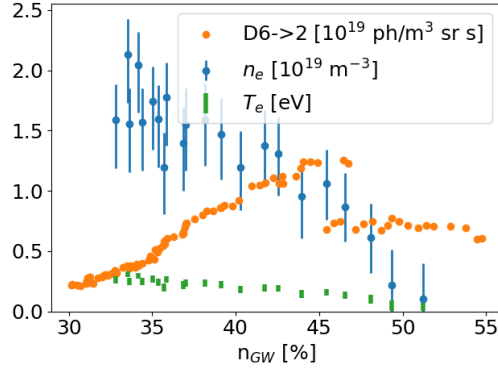


Figure 11: Comparison of the electron density and 9→2 Balmer emission (proxy for the electron-ion recombination) front detachment at 3 cm from the target along the separatrix, along with the inferred electron temperature.

here used as a proxy for the electron-ion recombination (EIR) region. The electron temperature inferred using the electron density from CIS and assuming that the Balmer emission is purely due to EIR is also shown, obtained as a solution of

$$\epsilon_{D6 \rightarrow 2}(n_e, T_e) = n_e^2 PEC_{rec}(n_e, T_e) \quad (1)$$

with the PEC effective emission coefficients taken from the ADAS database. This delay between the detachment of the two fronts is attributed to the conditions of the MAST-U divertor, with low electron densities and low electron temperatures ( $\leq 0.5$  eV). In these conditions, the amount of EIR is mostly driven by the low temperatures, as also observed in interpretative simulations [23], instead of by the dependency on electron density. As the divertor becomes more detached, the density front starts moving away from the target, which drives down the amount of the EIR, but the simultaneous decrease in electron temperature drives more EIR emission. The balance of the two effects results in a delayed detachment of the EIR front compared to the electron density front. This delay might be less visible in higher density conditions, where the amount of EIR is mostly driven by its density dependence ( $\propto n_e^3$ ).

#### 4.2 Comparison with analytical models

The behavior of the density near the target can be used in conjunction with reduced analytical models to infer the increase in total power and momentum losses with increasing total flux expansion and the volume available for plasma-neutral interactions. The modified 2-point model [28] can be used to relate upstream conditions, characterized by the parallel heat flux  $q_{||,u}$  and total pressure  $p_{tot,u}$ , to the target electron density, temperature and particle flux through power and momentum balance along a flux tube. Power and momentum losses along the flux tube (e.g. from volumetric and

cross-field transport effects) are expressed through fractional loss terms,  $f_{cool}$  and  $f_{mom}$  respectively.

$$T_t^{2PM} = \frac{8m_i}{\gamma^2} \frac{q_{||,u}^2}{p_{tot,u}^2} \frac{(1-f_{cool})^2}{(1-f_{mom})^2} \left(\frac{R_u}{R_t}\right)^2 \quad (2)$$

$$n_t^{2PM} = \frac{\gamma^2}{32m_i} \frac{p_{tot,u}^3}{q_{||,u}^2} \frac{(1-f_{mom})^3}{(1-f_{cool})^2} \left(\frac{R_u}{R_t}\right)^{-2} \quad (3)$$

$$\Gamma_t^{2PM} = \frac{\gamma}{8m_i} \frac{p_{tot,u}^2}{q_{||,u}} \frac{(1-f_{mom})^2}{(1-f_{cool})} \left(\frac{R_u}{R_t}\right)^{-1} \quad (4)$$

The effects of total flux expansion are explicitly accounted for by the ratio in the upstream and target major radii,  $R_u$  and  $R_t$ , assuming that the magnetic field strength decays radially  $B \propto R^{-1}$ , which is well met in the equilibria considered for this work. The lack of simple models for  $f_{cool}$  and  $f_{mom}$  during detachment makes a comparison of the absolute density measurements against the model difficult. However, these losses incurred before reaching the target can be estimated experimentally by putting together the electron density measured near the target by the CIS with the peak particle flux measured by the target Langmuir probes for the same upstream conditions. Taking the ratio of eq (3) in SXD and ED for the same upstream pressure and substituting in the ratio of eq (4) for the two configurations gives

$$\frac{(1-f_{cool})_{SXD}}{(1-f_{cool})_{ED}} = \frac{\Gamma_{SXD}^3}{\Gamma_{ED}^3} \frac{n_{e,SXD}^{-2}}{n_{e,ED}^{-2}} \frac{R_{SXD}}{R_{ED}} \quad (5)$$

$$\frac{(1-f_{mom})_{SXD}}{(1-f_{mom})_{ED}} = \frac{\Gamma_{SXD}^2}{\Gamma_{ED}^2} \frac{n_{e,SXD}^{-1}}{n_{e,ED}^{-1}} \quad (6)$$

These equations express the ratio in power and momentum reaching the target in the SXD compared to the ED. Similar equations can be found using an extension of the 2-point model that accounts for possible momentum losses due to total flux expansion in the presence of significant plasma flows [15]. In this case, the momentum loss term can be divided between a term accounting for volumetric and cross-field momentum losses ( $1-f_{mom}^S$ ) and a term accounting for geometric losses, which is a function of the effective Mach number  $M_{eff}$ , thus

$$(1-f_{mom}) = (1-f_{mom}^S) \left(\frac{R_u}{R_t}\right)^{\frac{M_{eff}^2}{1+M_{eff}^2}} \quad (7)$$

Assuming the value of  $M_{eff}$  does not vary significantly between the ED and SXD configurations, the ratio of the volumetric and cross-field momentum losses can be expressed explicitly as

$$\frac{(1-f_{mom}^S)_{SXD}}{(1-f_{mom}^S)_{ED}} = \frac{\Gamma_{SXD}^2}{\Gamma_{ED}^2} \frac{n_{e,SXD}^{-1}}{n_{e,ED}^{-1}} \left(\frac{R_{SXD}}{R_{ED}}\right)^{\frac{M_{eff}^2}{1+M_{eff}^2}} \quad (8)$$

While experimental values of  $M_{eff}$  are not available, 3 limiting cases can be considered:

- A case where the effect of flows are not significant ( $M_{eff} = 0$ ), leading to no additional momentum losses and the original 2PM equation (6)

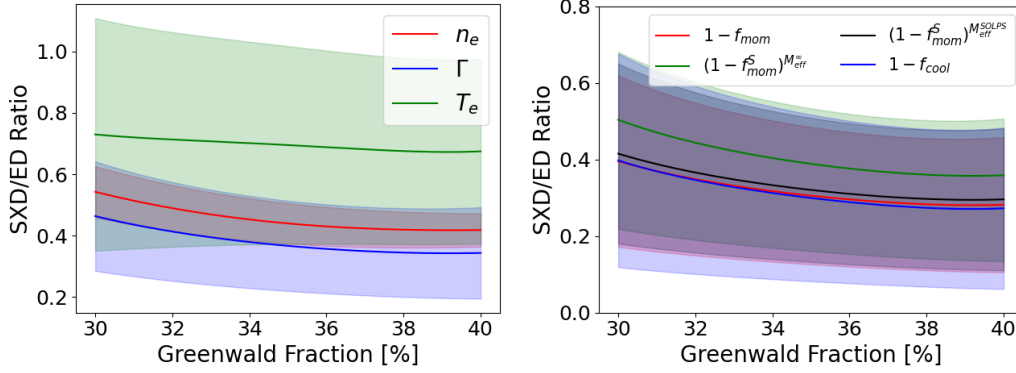


Figure 12: Ratio of inferred target quantities (a) and integrated momentum and power losses (b) in the SXD and ED configuration.

- A case using a characteristic  $M_{eff}$  value computed from interpretative SOLPS simulations of the discharges (explored more in section 4.3) ( $M_{eff}^{SOLPS} \sim 0.5$ )
- A case which maximises the effect of geometric losses and minimizes the volumetric effects ( $M_{eff}^{\infty} \rightarrow \infty$ )

The inferred target electron density and particle flux ratios between the SXD and ED during the NBI heated core density ramps are shown in figure 12a as a function of core Greenwald fraction, along with the  $T_e$  ratio that can be inferred from the other two measurements assuming sounds speed at the target as in the traditional 2 point model.

$$\frac{T_e^{SXD}}{T_e^{ED}} = \frac{\Gamma_{SXD}^2 n_{e,SXD}^{-2}}{\Gamma_{ED}^2 n_{e,ED}^{-2}} \quad (9)$$

The target electron density and particle flux are lower in the SXD by about 50 % and 60 % compared to their values in ED respectively. The inferred power ( $1 - f_{cool}$ ) and momentum ( $1 - f_{mom}$ ) reaching the target are  $\sim 70$  % smaller in SXD than the ones in ED, as shown in figure 12b, evidence of the significant improvement in performance with increasing leg-length. The particle flux, electron density, power losses and momentum losses ratios all show a slightly decreasing trend towards higher upstream densities. This suggests that the increased benefits from long-legged configurations are stronger in more deeply detached conditions, probably due to the increased role of volumetric losses. The strong increase in momentum losses in MAST-U is much larger than what would be expected from geometric effects alone. Using  $M_{eff}$  from SOLPS leads to  $\sim 95$  % of the increase in momentum losses being attributed to volumetric and cross-field effects, while even in the limit case  $M_{eff}^{\infty}$  this value is still of  $\sim 79$  %. A similar type of analysis can be applied to the poloidal leg scan with constant upstream conditions. In this case, the inferred values are normalized to the initial value of the scan, with the strike point major radius at 1.15 m. As the leg is swept out, both the target electron density and the particle flux are inferred to decrease by  $\sim 50$  %, as shown in figure 13a. It is worth noting that in this case, the drop in particle flux is slightly smaller than in the comparison of the core density ramps, which can be attributed to slightly different upstream conditions between the two compared density ramps. The momentum and power reaching the target are shown in figure 13b and they are inferred to strongly decrease from their initial values as the leg is swept out, leading to a  $\sim 60$  % reduction in both power and momentum. In this case, volumetric and

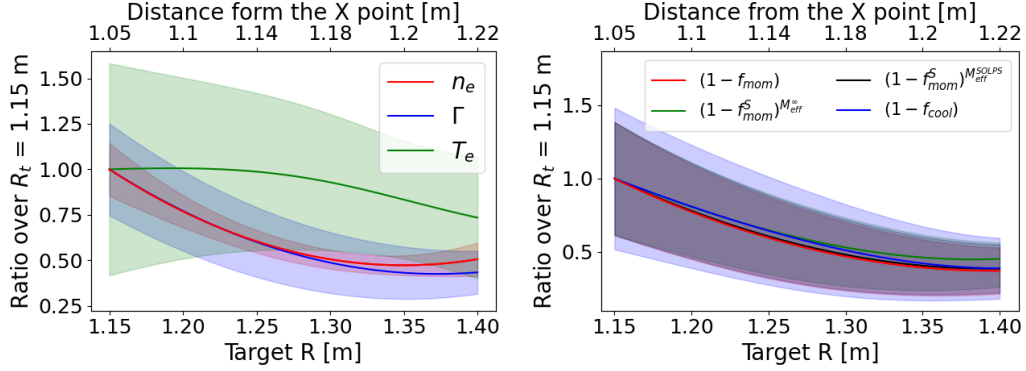


Figure 13: Ratio of inferred target quantities (a) and integrated momentum and power losses (b) as the leg is swept from ED to a larger target radius.

cross field momentum losses are inferred to dominate over the geometric momentum losses over the entire scan, making up average values of 97 % and 90 % of the momentum losses in the  $M_{eff}^{SOLPS}$  and  $M_{eff}^{\infty}$  respectively.

#### 4.3 Comparison with SOLPS simulations

The inferred electron density profiles can be compared against the profiles from interpretative SOLPS simulations of these discharges to validate the capabilities of the code in the strongly baffled long-legged conditions available on MAST-U. To account for possible artifacts and systematic errors that can appear during the tomographic inversion to obtain the 2D profiles, the measurements are also compared to "synthetic" 2D profiles (with their respective uncertainties) obtained by using the SOLPS profiles to generate synthetic CIS data, which is then tomographically inverted as previously done to characterize the performance of the diagnostic [18].

The 2D  $n_e$  profile obtained from the interpretative simulation, including drifts, of ED discharge #47079 with a simulated power crossing the separatrix of  $P_{SOL}^{SOLPS} = 1$  MW is shown in figure 14, along with the comparison between the experimental and simulated electron density profiles along the separatrix. Analogously, the cross-field profiles are compared at 5 and 20 cm from the target in figure 15. Overall, there is good agreement with the interpretative simulation in both the magnitude and shape of the profiles. While the experimental profile is inferred to be slightly decreasing downstream of the density maximum near the detachment front, the profile is still in agreement within uncertainty with the simulated profile which is peaked at the target. While the agreement between experimental and simulated profiles is reasonable, the cross-field synthetic SOLPS profile shows an underestimation of the density in the PFR near the target, suggesting a possible limitation of the camera view when trying to reconstruct the behavior in the narrow gap between the separatrix and the tile in this magnetic geometry.

The profiles are less in agreement in the SXD case, where the experimental profile shows a higher density along the separatrix which quickly falls off in the private flux region (PFR), while the SOLPS simulations predict a broader profile with significant spreading in the PFR and a lower maximum density. Contrary to expectations, better agreement can be found with simulations without drifts, which predict a sharper drop-off of the density in the PFR and a higher peak density. The 2D  $n_e$  profiles from SOLPS simulations with drifts enabled and disabled are

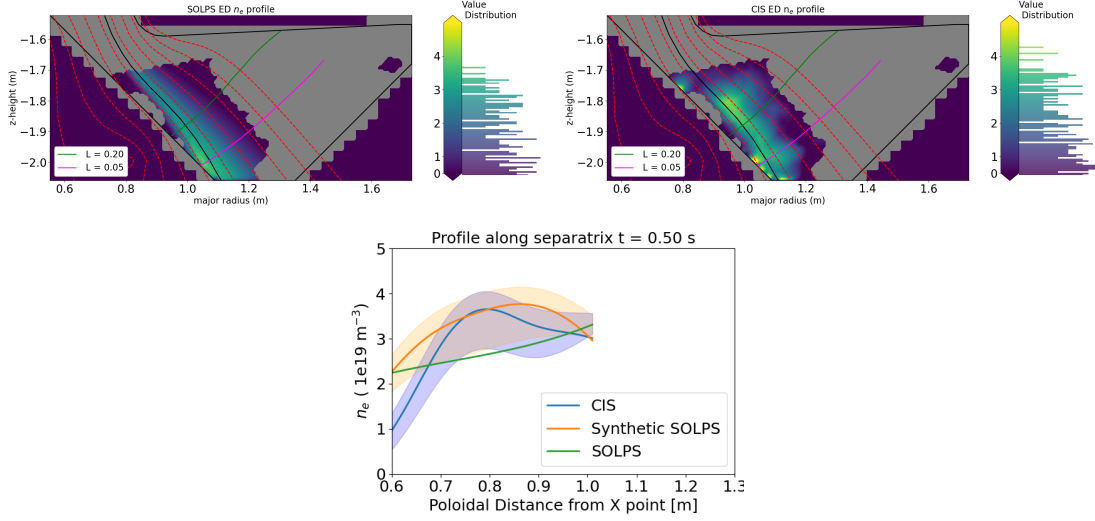


Figure 14: (a)  $n_e$  profile from an interpretative SOLPS simulation of ED NBI-heated shot #47079. (b) Experimental profile matching the same upstream density (c) Comparison of experimental, simulated, and synthetic electron density profiles along the separatrix.

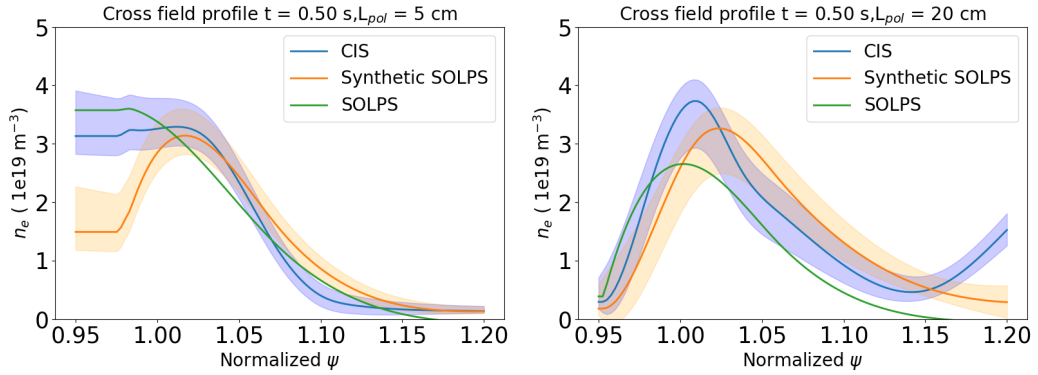


Figure 15: Comparison of experimental, simulated, and synthetic electron density profiles across the separatrix at 5 cm (a) and 20 cm (b) from the target in ED discharge 47079.

shown in figure 16, which can be compared to the experimental inferred profile in figure 4. This suggests that the effect of drifts may be over-estimated in these simulations and future comparison in attached conditions may be able to indicate if this is related specifically to the longer-legged geometry or to the temperature range achieved in these detached conditions. The profile along the separatrix doesn't match as well as in the ED case with either simulation, as shown in figure 17. The experimental profile shows a peak in the middle of the divertor chamber and then a significant decrease in density toward the target. This behaviour is not in agreement with the SOLPS simulations, that predict a monotonically increasing density in either simulation with and without drifts. A possible explanation for this behavior is a smaller amount of neutral drag in experiment compared to the simulations, which could be due to the larger divertor neutral pressure

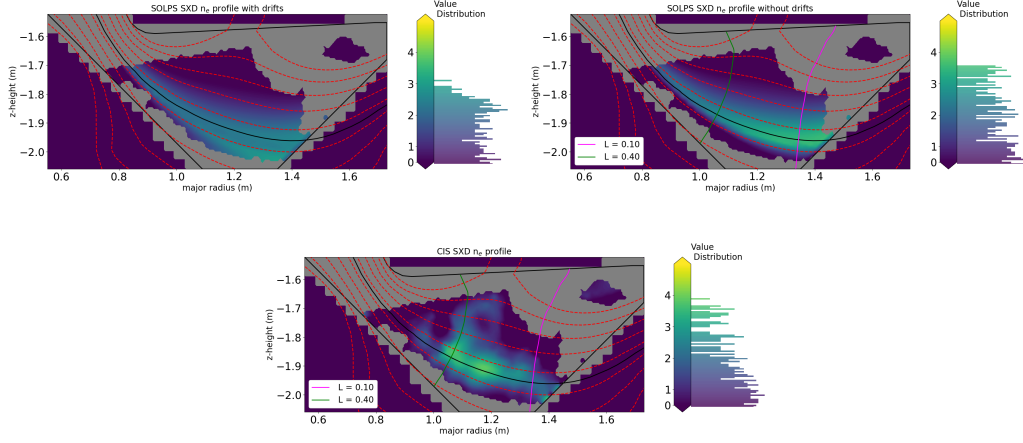


Figure 16: 2D  $n_e$  profiles from interpretative simulations of SXD discharge #46860 with drifts (a) enabled and (b) disabled. (c) Experimentally inferred profile.

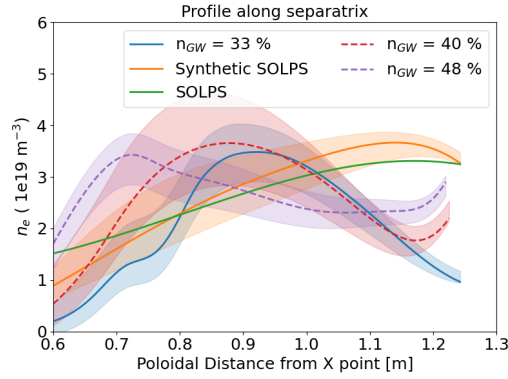


Figure 17: Comparison of experimental, simulated, and synthetic electron density profiles along the separatrix with interpretative simulations without drifts of SXD discharge #46860. The upstream density matches the simulations for  $n_{GW} = 33\%$ , while later points are shown as the agreement improves when the upstream density is higher.

predicted by SOLPS compared to experiment ( $\sim 1 \text{ Pa}$  vs  $\sim 0.3 \text{ Pa}$ ), or to the SOLPS model not fully capturing the momentum loss processes. Better agreement is obtained if the simulated profiles are compared to later times during the core density ramps, as the experimental density profiles flattens in the divertor chamber. Even though in this case the comparison is not performed for the same upstream density anymore, the inferred peak density in the divertor does not change significantly, just moving upstream and flattening after the peak. This is attributed to the deeply detached conditions already present at the start of the discharge, suggesting that the total amount of ionization does not increase significantly during the discharge. Instead, the ionization front, downstream of which the electron temperature becomes too low to ionize additional neutrals, moves further upstream as this same amount of ionization is produced in a shorter amount of space. The cross-field profile is shown at 20 cm from the target in figure 18, where it can be seen the reasonable

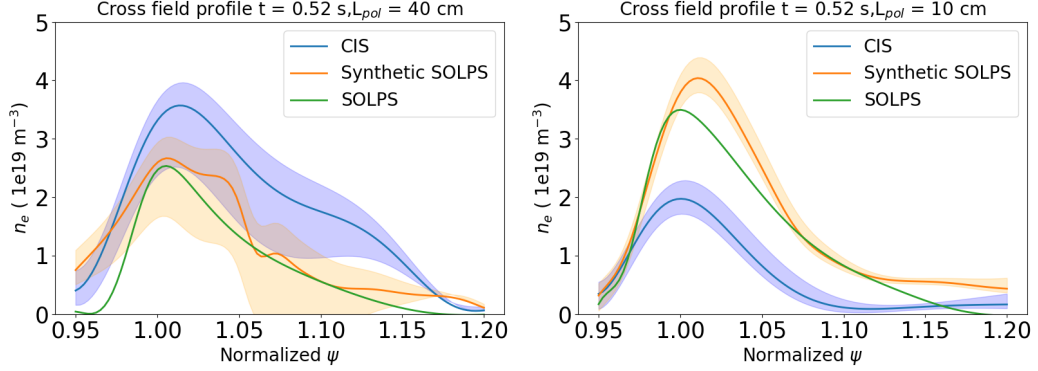


Figure 18: Comparison of experimental, simulated (without drifts), and synthetic electron density profiles across the separatrix at 20 cm (a) and 10 cm (b) from the target in SXD discharge #46860.

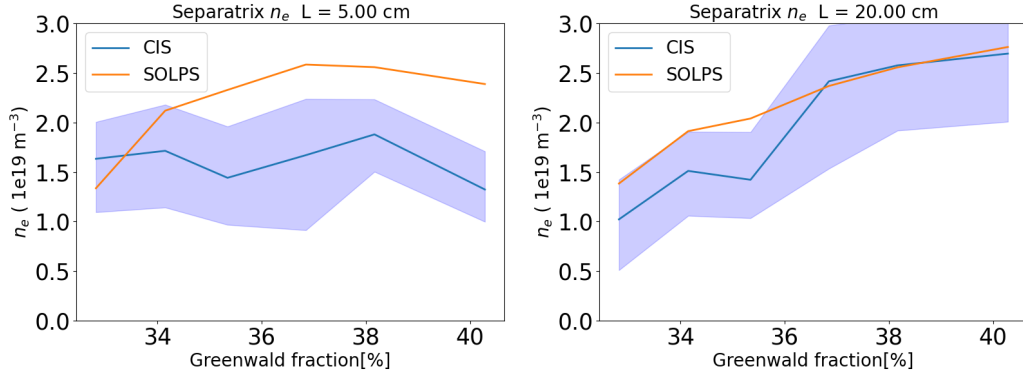


Figure 19: Comparison of inferred and simulated electron density along the separatrix at 5 (a) and 20 (b) cm from the target as a function of upstream density in Ohmic conditions.

agreement with the simulations, in particular regarding the sharp drop in the PFR and the peak density. Worse agreement is found in the peak density closer (10 cm) to the target, although the width of the profile is still in reasonable agreement.

Inferences in the Ohmic case are complicated by the lower electron densities, increasing the uncertainty of the Stark-broadening-based measurements, and making a detailed comparison of the profile along and cross the separatrix less reliable. Furthermore, numerical instabilities are observed in the SOLPS simulations after the electron density front detaches from the target. In this case, the comparison has been limited to the values on the separatrix and close to the target, where the densities are highest and the inference more reliable, up until the density front detaches from the target in the simulations. The inferred densities along the separatrix at 5 and 20 cm from the target are compared with increasing upstream density with a series of SOLPS simulations with  $P_{SOL} = 0.6 \text{ MW}$  and increasing fuelling rate in figure 19. The inferred density is in reasonable agreement throughout the density scan up to the density front detachment, albeit the density very close to the target is slightly underestimated, as observed in the NBI-heated case.



#### 4.4 Neutral drag and electron density build-up near the target

The evolution of the electron density profile downstream of the detachment front is in qualitative agreement with simple modeling based on the competition of neutral drag, which increases the electron density, and recombination ion sinks, which decrease it.

Considering a 1D model along a flux tube and neglecting cross-field transport, the density at each point will be given by the solution of the continuity equation. Focusing on the region downstream of the detachment front, where negligible ionization is assumed, the density at each point (T) will be a function of the density at the detachment front (DF), the integrated volumetric recombination between the front and the point and the flow velocities at the detachment front and the point T

$$\frac{d}{dx} [n_e(x)v(x)] = -S_{rec}(x)$$

$$n_e^{DF} v^{DF} - n_e^T v^T = - \int_T^{DF} S_{rec}(x) dx \quad (10)$$

Given the lack of ionization downstream of the detachment front and the presence of strong volumetric particle sinks in the MAST-U divertor [20], which would tend to lower the electron density, another mechanism must be present to increase it. A possible explanation is that a strong drop in parallel velocity must be present, which has also been observed in interpretative SOLPS simulations of the Super-X divertor and has been attributed to ion-molecule collisions [23].

The non-monotonic behaviour at the start of the SXD discharge can then be understood as MAR recombination processing dominating over the neutral drag near the target. As the density ramp progresses, the neutral pressure in the divertor rises, increasing the drag and resulting in a flattening of the electron density profile or even a peaking at the target. The increase in neutral pressure also leads to a reduction in the electron temperature which promotes electron-ion recombination in later stages of the discharge [20]. Eventually, the electron-ion recombination losses become strong enough to dominate over the effect of the neutral drag and cause a reduction of the electron density near the target and the movement of the electron density front away from the target, as observed experimentally in Ohmic conditions (figure 10).

To try and show this behaviour qualitatively, the continuity equation can be solved numerically as a function of electron temperature through a change of variables

$$n_e^{DF} v^{DF} - n_e^T v^T = - \int_{T_e^T}^{T_e^{DF}} S_{rec}(T_e) \frac{dx}{dT_e}(T_e) dT_e$$

and by expressing the volumetric particle sinks in terms of the effective rates for electron-ion recombination (ACD) and molecular activated recombination (MAR). The increase in volume available for recombination due to total flux expansion can be accounted for by in the assumption  $|B| \propto 1/R$  by multiplying the sink term by the ratio in major radius

$$n_e^{DF} v^{DF} - n_e^T v^T(T_e) = - \int_{T_e^T}^{T_e^{DF}} (ACD(n_e, T_e) n_e^2 + MAR(n_e, T_e) n_e D_2(T_e)) \frac{dx}{dT_e}(T_e) \frac{R(T_e)}{R(T_e^{DF})} dT_e$$

where the values of  $n_e^{DF}$ ,  $v(T_e)$ ,  $D_2(T_e)$  and the temperature gradient  $\frac{dT}{dx}(T_e)$  are taken from the respective interpretative SOLPS simulation.

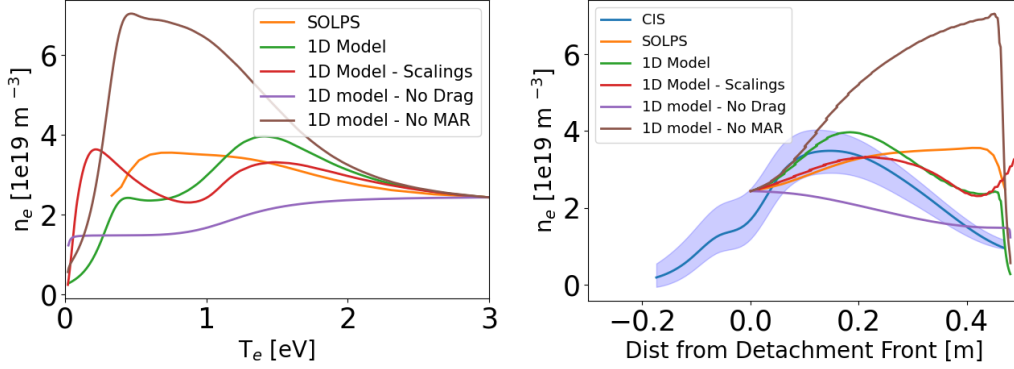


Figure 20: Comparison of SOLPS  $n_e$  profile with the results of the 1D model taking the information from SOLPS and the 1D model using the simplified scaling laws. Plotted against  $T_e$  (left) and poloidal distance downstream of the detachment front (right).

The equation can then be solved numerically iteratively by starting from the detachment front (assumed as a temperature front at  $T_e^{DF} = 3$  eV) and taking steps towards lower temperatures

$$n_e^{i+1}(T_e + dT_e) = n_e^{DF} \frac{v^{DF}}{v^{i+1}(T_e + dT_e)} + \frac{1}{v^{i+1}(T_e + dT_e)} \sum_{j=0}^{i+1} \left( ACD(n_e^j, T_e^j) (n_e^j)^2 + MAR(n_e^j, T_e^j) n_e^j D_2(T_e^j) \right) \frac{dx}{dT_e}(T_e^j) \frac{R(T_e^j)}{R(T_e^{DF})} dT_e$$

This leads to the non-monotonic behaviour shown in figure 20, with the density increasing downstream of the detachment front up to 1.5 eV and then decreasing at lower temperatures. The second peak at 0.5 eV is in an intermediate temperature range, where the MAR particle losses become less significant but the temperature is still too high for significant EIR losses. The profile can also be compared to the solution obtained assuming no drag (i.e.  $v^{DF} = v^T$ ), where the density monotonically decreases downstream of the front, and to the solution neglecting MAR losses, which reaches significantly higher peak densities, highlighting how both of these processes are necessary to obtain peak densities along the profiles comparable to the SOLPS results.

Using the same information on the temperature gradient used to solve the equation,  $\frac{dT}{dx}(T_e)$ , the curve can be expressed as a function of poloidal distance downstream of the detachment front, and thus directly compared to the experimentally inferred values, also shown in figure 20. Although the agreement with experiment is not perfect, the comparison suggest that a model based on the competition of neutral drag and volumetric particle sinks can produce non-monotonic electron density behaviour comparable in magnitude to what is observed in experiment. If the divertor densities are higher, the volumetric particle sinks will also increase and it is reasonable to expect that this non-monotonic density behaviour would become stronger and the density would not be able to rise again near the target at intermediate temperatures ( $T_e \leq 0.7$  eV) as EIR sinks would already be strong at those temperatures.

This behaviour can be qualitatively tested by interpolating the values of  $v(T_e, L_T)$ ,  $D_2/n_e(T_e, L_T)$  and  $\frac{dT}{dx}(T_e, L_T)$  from SXD SOLPS simulations at different heating powers as a function of electron temperature and parallel distance from the target ( $L_T$ ). The curves obtained by solving the equation using these interpolated scalings instead of the values taken directly from SOLPS are compared

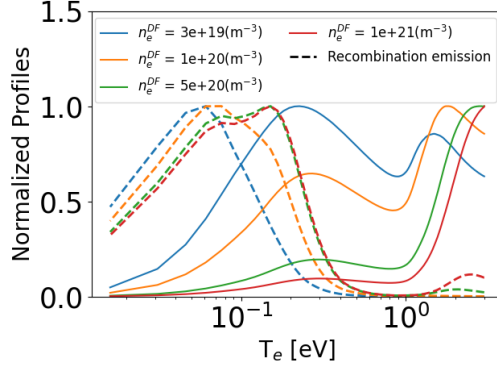


Figure 21: Comparison of  $n_e$  and  $D_\alpha$  EIR emissivity profiles normalized to their respective maxima, obtained by solving the 1D model extrapolation at higher density. The second peak at the target vanishes at higher densities due to the stronger sinks.

to the previous curves in figure 20. It can be noticed how the second density peak near the target is over-estimated, as the scaling does not fully capture the flattening of the parallel velocity very close to the target predicted by SOLPS.

Using these scalings and scanning the starting electron density at the detachment front leads to the results in figure 21. At low detachment front densities, the  $n_e$  profile has a second peak at the target, caused by the low amount of recombination until very low temperatures are reached ( $\leq 0.3$  eV). As the detachment front densities increases, so do the ion sinks and this behaviour is not observed. The peak density along the profile is now at the first local maxima, before MAR ions sinks lead to the decrease in density. The peak density along the profile keeps moving to higher electron temperatures as the electron density increases and suggests that the density front would be easier to detach from the target in higher density machines compared to MAST-U.

The  $n_e$  and  $T_e$  information can also be used to model the EIR emission for the  $D_\alpha$  Balmer line using eq (1). The  $n_e$  and  $\epsilon$  profiles normalized to their respective maxima are compared in figure 21. At low electron densities, the EIR emission is peaked at the target and starts decreasing (i.e. detaching from the target) at lower temperatures than the density front, as observed experimentally in MAST-U. At higher detachment front densities, the EIR emission presents two peaks, one corresponding to the density peak and one at low temperatures, which would be at the target if electron temperatures  $\leq 0.5$  eV can be achieved. The extrapolated behaviours at higher densities are in qualitative agreement with the behaviour reported on JET: a density peaking at the target at higher upstream densities (and lower temperatures) than the ion flux rollover, and a continuously decreasing target density after the maximum is reached. Furthermore, two peaks in recombination emission are observed in deep detachment, the first close to the maximum density (near the X-point) and the second one at the target driven by low electron temperatures [26].

## 5 Conclusions

The behavior of the 2D electron density profile in the MAST-U divertor has been characterized in L-mode discharges with varying strike point radius, upstream density and input power. As the divertor leg length and total flux expansion are increased, the power and momentum losses along the separatrix are inferred to strongly increase, resulting in decreasing target electron density and

particle flux and highlighting the increased exhaust performance of the Super-X divertor. As the divertor detachment state evolves, the electron density profile is inferred to peak downstream of the ionization front. This is attributed to the effect of neutral drag reducing the plasma flow and increasing the electron density. In early stages of detachment the peak is observed just downstream of the front, while in later stages the density peaks at the target. When low enough target temperatures are reached ( $T_e < 0.3$  eV) and the electron-ion recombination sinks start to dominate over the drag effect, resulting in the density front detaching from the target. Comparison of the inferred electron density profiles with interpretative SOLPS-ITER simulations shows generally reasonable agreement in the electron density profiles along and across the separatrix, albeit the experimentally inferred non-monotonic profile in the early stages of the Super-X density ramp is not well reproduced by SOLPS. The discrepancy is attributed to an over-estimation of the profile broadening in the private flux region due to drifts and either an overestimation of the effect of drag or underestimation of the particle sinks near the target, thus predicting a density profile peaked at the target. This experimentally inferred behaviour is in qualitative agreement with simple modelling of the density profile downstream of the detachment front as a balance between recombination particle sinks and neutral drag acting on the plasma. Extrapolating this model to higher electron density conditions than those available on MAST-U shows the density peak at low temperatures vanish, as the effect of ion sinks become stronger.

## 6 Acknowledgements

This work has been carried out within the framework of the EUROfusion Consortium, partially funded by the European Union via the Euratom Research and Training Programme (Grant Agreement No 101052200 — EUROfusion), and from EPSRC Grant EP/S022430/1. The Swiss contribution to this work has been funded by the Swiss State Secretariat for Education, Research and Innovation (SERI). Views and opinions expressed are however those of the author(s) only and do not necessarily reflect those of the European Union, the European Commission or SERI. Neither the European Union nor the European Commission nor SERI can be held responsible for them.

## References

- [1] Wenninger R, Bernert M, Eich T, Fable E, Federici G, Kallenbach A, Loarte A, Lowry C, McDonald D, Neu R, Pütterich T, Schneider P, Sieglin B, Strohmayer G, Reimold F and Wischmeier M 2014 *Nuclear Fusion* **54** 114003 URL <https://dx.doi.org/10.1088/0029-5515/54/11/114003>
- [2] Kotschenreuther M T, Valanju P M, Wiley J C, Rognlein T D, Mahajan S M and Pekker M 2004 Scrape off layer physics for burning plasmas and innovative divertor solutions URL <https://api.semanticscholar.org/CorpusID:44327246>
- [3] Ryutov D 2007 *Physics of Plasmas* **14** cited by: 269; All Open Access, Green Open Access URL <https://www.scopus.com/inward/record.uri?eid=2-s2.0-34547380960&doi=10.1063/2f1.2738399&partnerID=40&md5=283f27afc0e1b84c65984891748c176b>
- [4] Valanju P M, Kotschenreuther M, Mahajan S M and Canik J 2009 *Physics of Plasmas* **16** 056110 ISSN 1070-664X (*Preprint* [https://pubs.aip.org/aip/pop/article-pdf/doi/10.1063/1.3110984/14032310/056110\\_1\\_online.pdf](https://pubs.aip.org/aip/pop/article-pdf/doi/10.1063/1.3110984/14032310/056110_1_online.pdf)) URL <https://doi.org/10.1063/1.3110984>
- [5] LaBombard B, Marmor E, Irby J, Terry J, Vieira R, Wallace G, Whyte D, Wolfe S, Wukitch S, Baek S, Beck W, Bonoli P, Brunner D, Doody J, Ellis R, Ernst D, Fiore C, Freidberg J, Golfopoulos T, Granetz R, Greenwald M, Hartwig Z, Hubbard A, Hughes J, Hutchinson I, Kessel C, Kotschenreuther M, Leccacorvi R, Lin Y, Lipschultz B, Mahajan S, Minervini J, Mungaard R, Nygren R, Parker R, Poli F, Porkolab M, Reinke M, Rice J, Rognlien T, Rowan W, Shiraiwa S, Terry D, Theiler C, Titus P, Umansky M, Valanju P, Walk J, White A, Wilson J, Wright G and Zweben S 2015 *Nuclear Fusion* **55** 053020 URL <https://dx.doi.org/10.1088/0029-5515/55/5/053020>

- [6] Piras F, Coda S, Furno I, Moret J M, Pitts R A, Sauter O, Tal B, Turri G, Bencze A, Duval B P, Felici F, Pochelon A and Zucca C 2009 *Plasma Physics and Controlled Fusion* **51** 055009 URL <https://dx.doi.org/10.1088/0741-3335/51/5/055009>
- [7] Maurizio R, Tsui C K, Duval B P, Reimerdes H, Theiler C, Boedo J, Labit B, Sheikh U, Spolaore M, Team T T and Team T E M 2018 *Nuclear Fusion* **59** 016014 ISSN 0029-5515 publisher: IOP Publishing URL <https://dx.doi.org/10.1088/1741-4326/aaee1b>
- [8] Soukhanovskii V A, Cunningham G, Harrison J R, Federici F and Ryan P 2022 *Nuclear Materials and Energy* **33** 101278 ISSN 2352-1791 URL <https://www.sciencedirect.com/science/article/pii/S2352179122001594>
- [9] Verhaegh K, Lipschultz B, Harrison J, Osborne N, Williams A, Ryan P, Allcock J, Clark J, Federici F, Kool B, Wijkamp T, Fil A, Moulton D, Myatra O, Thornton A, Bosman T, Bowman C, Cunningham G, Duval B, Henderson S, Scannell R and the MAST Upgrade team 2022 *Nuclear Fusion* **63** 016014 URL <https://dx.doi.org/10.1088/1741-4326/aca10a>
- [10] Verhaegh K, Lipschultz B, Harrison J, Federici F, Moulton D, Lonigro N, Kobussen S, O'Mullane M, Osborne N, Ryan P, Wijkamp T, Kool B, Rose E, Theiler C, Thornton A and the MAST Upgrade Team 2023 *Nuclear Fusion* **63** 126023 URL <https://dx.doi.org/10.1088/1741-4326/acf946>
- [11] Verhaegh K, Harrison J R, Moulton D, Lipschultz B, Lonigro N, Osborne N, Ryan P, Theiler C, Wijkamp T, Brida D, Cowley C, Derks G, Doyle R, Federici F, Kool B, Février O, Hakola A, Henderson S, Reimerdes H, Thornton A J, Vianello N, Wischmeier M and Xiang L 2024 Improved divertor performance in strongly baffled, alternative divertors on mast upgrade (*Preprint* [2311.08586](https://arxiv.org/abs/2311.08586))
- [12] Moulton D, Harrison J R, Xiang L, Ryan P J, Kirk A, Verhaegh K, Wijkamp T A, Federici F, Clark J G and Lipschultz B 2024 *Nuclear Fusion* **64** 076049 ISSN 0029-5515 publisher: IOP Publishing URL <https://dx.doi.org/10.1088/1741-4326/ad4f9c>
- [13] Theiler C, Lipschultz B, Harrison J, Labit B, Reimerdes H, Tsui C, Vijvers W, Boedo J A, Duval B, Elmore S, Innocente P, Kruezi U, Lunt T, Maurizio R, Nespoli F, Sheikh U, Thornton A, van Limpt S, Verhaegh K, Vianello N, the TCV team and the EUROfusion MST1 team 2017 *Nuclear Fusion* **57** 072008 URL <https://dx.doi.org/10.1088/1741-4326/aa5fb7>
- [14] Theiler C, Février O, Reimerdes H, Thornton A, Baquero-Ruiz M, Berner M, Blanchard P, Brida D, Colandrea C, Oliveira H D, Dunne M, Duval B P, Fasoli A, Fil A, Frassinetti L, Galassi D, Gorno S, Harrison J, Henderson S, Komm M, Labit B, Linehan B, Lipschultz B, Martinelli L, Offeddu N, Perek A, Raj H, Sheikh U, Sun G, Tsui C K, Vincent B, Wensing M, Wuethrich C, Team T T and Team T E M *submitted to Nuclear Fusion*
- [15] Carpita M, Février O, Reimerdes H, Theiler C, Duval B, Colandrea C, Durr-Legoupil-Nicoud G, Galassi D, Gorno S, Huett E, Loizu J, Martinelli L, Perek A, Simons L, Sun G, Tonello E, Wüthrich C and the TCV Team 2024 *Nuclear Fusion* **64** 046019 URL <https://dx.doi.org/10.1088/1741-4326/ad2a2a>
- [16] Osborne N, Verhaegh K, Bowden M D, Wijkamp T, Lonigro N, Ryan P, Pawelec E, Lipschultz B, Soukhanovskii V, van den Biggelaar T and the MAST-U Team 2023 *Plasma Physics and Controlled Fusion* **66** 025008 URL <https://dx.doi.org/10.1088/1361-6587/ad1654>
- [17] Doyle R S, Lonigro N, Allcock J S, Silburn S A, Turner M M, Feng X and Leggate H 2024 *Review of Scientific Instruments* **95** 053505 ISSN 0034-6748 (*Preprint* [https://pubs.aip.org/aip/rsi/article-pdf/doi/10.1063/5.0205584/19947615/053505\\_1\\_5.0205584.pdf](https://pubs.aip.org/aip/rsi/article-pdf/doi/10.1063/5.0205584/19947615/053505_1_5.0205584.pdf)) URL <https://doi.org/10.1063/5.0205584>
- [18] Lonigro N, Doyle R, Allcock J S, Lipschultz B, Verhaegh K, Bowman C, Brida D, Harrison J, Myatra O, Silburn S, Theiler C, Wijkamp T A, Team M U and the EUROfusion Tokamak Exploitation Team 2024 First 2d electron density measurements using coherence imaging spectroscopy in the mast-u super-x divertor (*Preprint* [2404.12021](https://arxiv.org/abs/2404.12021)) URL <https://arxiv.org/abs/2404.12021>
- [19] Wijkamp T A, Allcock J S, Feng X, Kool B, Lipschultz B, Verhaegh K, Duval B P, Harrison J R, Kogan L, Lonigro N, Perek A, Ryan P, Sharples R M, Classen I G J, Jaspers R J E and team t M U 2023 *Nuclear Fusion* **63** 056003 ISSN 0029-5515 publisher: IOP Publishing URL <https://dx.doi.org/10.1088/1741-4326/acc191>
- [20] Verhaegh K, Harrison J R, Lipschultz B, Lonigro N, Kobussen S, Moulton D, Osborne N, Ryan P, Theiler C, Wijkamp T, Brida D, Derks G, Doyle R, Federici F, Hakola A, Henderson S, Kool B, Newton S, Osawa R, Pope X, Reimerdes H, Vianello N and Wischmeier M 2024 Investigations of atomic & molecular processes of nbi-heated discharges in the mast upgrade super-x divertor with implications for reactors (*Preprint* [2311.08580](https://arxiv.org/abs/2311.08580))
- [21] Lipschultz B, Parra F I and Hutchinson I H 2016 *Nuclear Fusion* **56** 056007 URL <https://dx.doi.org/10.1088/0029-5515/56/5/056007>
- [22] Cowley C, Lipschultz B, Moulton D and Dudson B 2022 *Nuclear Fusion* **62** 086046 URL <https://dx.doi.org/10.1088/1741-4326/ac7a4c>
- [23] Myatra O, Moulton D, Dudson B, Lipschultz B, Newton S, Verhaegh K and Fil A 2023 *Nuclear Fusion* **63** 076030 ISSN 0029-5515 publisher: IOP Publishing URL <https://dx.doi.org/10.1088/1741-4326/acd9da>
- [24] Lomanowski B A, Meigs A G, Sharples R M, Stamp M and C G 2015 *Nuclear Fusion* **55** 123028 ISSN

- 0029-5515 publisher: IOP Publishing URL <https://doi.org/10.1088/0029-5515/55/12/123028>
- [25] Verhaegh K, Lipschultz B, Duval B, Harrison J, Reimerdes H, Theiler C, Labit B, Maurizio R, Marini C, Nespoli F, Sheikh U, Tsui C, Vianello N and Vijvers W 2017 *Nuclear Materials and Energy* **12** 1112–1117 ISSN 2352-1791 proceedings of the 22nd International Conference on Plasma Surface Interactions 2016, 22nd PSI URL <https://www.sciencedirect.com/science/article/pii/S2352179116301740>
- [26] Karhunen J, Lomanowski B, Solokha V, Aleiferis S, Carvalho P, Groth M, Kumpulainen H, Lawson K, Meigs A and Shaw A 2020 *Nuclear Materials and Energy* **25** 100831 ISSN 2352-1791 URL <https://www.sciencedirect.com/science/article/pii/S2352179120301022>
- [27] Feng X, Calcines A, Sharples R M, Lipschultz B, Perek A, Vijvers W A J, Harrison J R, Allcock J S, Andrebe Y, Duval B P, Mumgaard R T, MAST-U Team and EUROfusion MST1 Team 2021 *Review of Scientific Instruments* **92** 063510 ISSN 0034-6748, 1089-7623 URL <https://aip.scitation.org/doi/10.1063/5.0043533>
- [28] Stangeby P C 2018 *Plasma Physics and Controlled Fusion* **60** 044022 URL <https://dx.doi.org/10.1088/1361-6587/aaacf6>